PHILOSOPHICAL TRANSACTIONS A

Hydrogen enhanced cracking revealed by in-situ micro-cantilever bending test inside Environmental Scanning Electron Microscope

Journal:	*Philosophical Transactions A*
Manuscript ID	RSTA-2017-0106
Article Type:	Research
Date Submitted by the Author:	28-Feb-2017
Complete List of Authors:	Deng, Yun; Norges teknisk-naturvitenskapelige universitet, Department of Mechanical and Industrial Engineering Hajilou, Tarlan; Norges teknisk-naturvitenskapelige universitet, Department of Mechanical and Industrial Engineering Barnoush, Afrooz; Norges teknisk-naturvitenskapelige universitet, Department of Mechanical and Industrial Engineering
Issue Code: Click here to find the code for your issue.:	DM0117
Subject:	Materials science < ENGINEERING AND TECHNOLOGY, Mechanical engineering < ENGINEERING AND TECHNOLOGY, Electron Microscopy (64) < CHEMISTRY (1002), Environmental Chemistry (67) < CHEMISTRY (1002)
Keywords:	hydrogen embrittlement, iron aluminides (FeAl), fracture, in-situ test

Hydrogen enhanced cracking revealed by in-situ micro-cantilever bending test inside Environmental Scanning Electron Microscope

Yun Deng, Tarlan Hajilou, Afrooz Barnoush

Abstract:

In order to evalutate the hydrogen (H)-induced embrittlement in iron aluminum intermetallics, especially the one with stoichiometric composition of 50 at.% Al, a novel in-situ micro-cantilever bending test was applied within environmental scanning electron microscope, which provides both a full process monitoring and a clean, in-situ H-charging condition. Two sets of cantilevers were analyzed in this work: one set of un-notched cantilevers, and the other set with FIB-milled notch laying on two crystallographic planes: (010) and (110). The cantilevers were tested under two environmental conditions: Vacuum (~$5X10^{-4}$ Pa) and ESEM (450 Pa water vapor). Crack initiation at stress-concentrated locations and propagation to cause catastrophic failure were observed when cantilevers were tested in the presence of H; while no cracking occurred when tested in Vacuum. Both the bending strength for un-notched beams and the fracture toughness for notched beams were reduced under H exposure. The hydrogen embrittlement (HE) susceptibility was found to be orientation dependent: the (010) crystallographic plane was more fragile to HE than the (110) plane.

Keywords: hydrogen embrittlement; iron aluminides (FeAl); fracture; in-situ test

1. Introduction

1.1. Hydrogen embrittlement mechanism

Hydrogen (H), as a possible future energy source to replace the present fossil fuels, is gaining an increasing attention nowadays as “hydrogen economy”. However, the mechanical degradation that happens to most metallic materials when exposed to the H-contained environment has mostly retarded the development of such economy. Since it is first reported in 1875 by Johnson (1), quite much research has been done on investigating the underlying mechanisms, and different models were proposed based on various experimental observations and numerical simulations. Of all these possibilities, some are quite evident to discover, while some are only hypotheses that need to be experimentally validated. For example, for hydride-forming systems, such as Group IV elements, some Titanium (2) and Zirconium (3-6) alloys, the hydride forming and cleavage mechanism is widely accepted. For non-hydride-forming systems, the following three mechanisms have received widespread supports along with many doubts:

1) H-enhanced decohesion (HEDE), which was proposed by Troiano in the 1960s(7), simply postulated that the H accumulated at the crack tip, reduces the cohesive bond energy between atoms, thus decreasing the work needed for fracture to occur. Many in-directly experimental observations were published to support the HEDE mechanism. The crack tip opening angle decreases with rising H pressure in Fe-3Si (wt.%) alloy and Ni single crystals(8, 9); and intergranular fracture was promoted under H exposure (10, 11).

2) Adsorption induced dislocation emission (AIDE) states that the formation energy of dislocations at crack tips is reduced by hydrogen adsorbed at the crack surface, after which crack propagation is prompted by dislocation motion(12, 13). This mechanism is mainly based on the posterior interpretation of the morphological features on the fracture surface in terms of plasticity.
3) H induced localized plasticity (HELP) was proposed mainly based on the in-situ observation of dislocation motion inside environmental transmission electron microscope (ETEM) cells(14). From these observations, the solid solution H increases the dislocation mobility or decreases the stacking fault energy. These mechanisms will introduce local plasticity and strain softening, and thus explain the hydrogen-enhanced plastic failure.

Most of these possibilities, which are mainly obtained from the interpretation of the post-mortem morphological features from macroscopic tests, are in lack of some supporting evidence from direct experimental observations, or/and are primarily supported by simulations and models with several simplifications that remain to be validated. The HELP mechanism, as an exception, is largely built on in-situ observations of the dislocation motion in ETEM cells. As a descriptive mechanism, the HELP finds widespread supports since its first announcement. However, there are still oppositional voices. Song and Curtin (15, 16) proposed that hydrogen reduces dislocation mobility rather than enhances it based on atomic calculations. And recently, an opposite observation was published from ETEM cell that dislocations will be locked under H exposure, and the authors argued that the locking effect is caused by hydrogenated vacancy rather than atomic H (17). This brings another hot and yet under debating mechanism about H and strain assisted vacancy production(18). These mechanisms are H concentration, loading condition and material dependent, and are not necessarily mutually exclusive.

1.2. FeAl intermetallics

FeAl (B2) phase is of particular research interest for its rather simple crystal structure and its variety of defects: vacancies, anti-site atoms, anti-phase boundaries, etc. Besides that, due to their excellent corrosion resistance, low material cost, conservation of strategic elements, and relatively low density when compared with stainless steels (19-21), the FeAl intermetallic alloys are considered for many potential applications, for example, as structural materials to serve in high temperature and/or hostile environments (20, 22). However, limited ductility at ambient temperatures and a sharp drop in strength above 600 ^{o}C have largely retarded those applications. Studies have shown that the ductility decrease in many intermetallic alloy systems that contain a large amount of reactive elements, such as Al, Si and Ti, was due to their chemical reaction with water molecules:

$$2Al + 3H_2O = Al_2O_3 + 6H^+ + 6e^-$$

The produced chemisorbed H diffuses to the crack tip and results in the so-called hydrogen embrittlement (HE). Among several kinematic parameters involved in this process, the moisture/aluminide reaction kinetics and the H diffusion rate, are the crucial ones to influence the severity of the embrittlement. Several theoretical and experimental works have shown that a small addition of alloying elements, such as B and C, can work as a

remedy for HE susceptibility of these alloys (23-25). The grain boundaries in Al-rich FeAl alloys with B2 structure were found to be intrinsically weak to lead to intergranular fracture even without H, while being B-doped, they became less brittle that fracture took place in a transgranular manner(26). However, even with addition of B, these alloys still suffered severe environmental embrittlement in the presence of H (27). It is also reported that C present in these alloys may enhance the ductility by forming carbides and trapping H within the carbide matrix interfaces (25, 28). The benefits achieved by adding C in Fe_3Al with $D0_3$ structure, however, cannot be achieved in FeAl with B2 structure because of the precipitation of soft graphite phase(24). The HE affects not only the fracture properties but also the fracture planes. For FeAl alloys with stoichiometric composition, the fracture was found to be along {111} plane when tested in oxygen while along {100} plane when tested in air(29). Fu and Painter(30) proposed that the segregation of H on the {100} plane will largely reduce the cleavage energy based on first-principles calculations. Li and Liu(31) suggested the H will promote the formation of <100> edge dislocations, which serves as crack nuclei for {100} cleavage. No common agreements have been achieved on the underlying mechanism.

One of the major reasons for the endless arguments of HE mechanisms is the lack of a proper experimental design. The previous experimental methods are either macroscopic tests overlooking the active length scale of H with crystal defects, or nano-scale tests inside ETEM with tiny sample size that cannot ensure a certain constant strain/stress states and cannot avoid the proximity effect from the sample surface. The recently works (32, 33) of micro-cantilever bending tests with in-situ hydrogen charging provide a good compromise by using the micro-sized sample that meet both the small scale required to capture the H effect and the enough bulk size to avoid the shortages from ETEM.

2. Experimental Procedure

2.1. Material and cantilever fabrication

The single crystalline FeAl alloy received from the Max-Planck-Institut Für Eisenforschung GmbH (MPIE) was grown by a modified Bridgman technique in BN-crucibles under argon atmosphere. <100> orientated seeds were used for the growth of single crystal with a diameter of 27 mm and a length of 80-100 mm in the growth direction. Small rectangular shaped specimen was cut by spark erosion, and the surface for manufacturing micro-cantilevers was finalized by electro-polish with a sulphic acid methanol base solution to ensure a defect-free state. The B2 ordered phase and the orientation of the specimen were characterized with Electron Backscattered Diffraction (EBSD). The Focused Ion Beam (FIB) (Helios Nanolab Dual Beam FIB, FEI Inc., USA) was used to mill micronized cantilevers. A final 90 pA current under 30 kV voltage was applied to maintain a good surface quality. The notch on the cantilever was milled with even lower current of 9 pA to achieve a sharp end. Fig.1 shows the geometry and the orientation of the cantilevers tested in this work. For un-notched cantilevers, the rectangular cross-sectional beams were manufactured with cubic orientation shown with the inset crystal model. For notched cantilevers, the pentagonal cross-section was chosen for its easy fabrication on surface, which gives the flexibility to select a desired beam orientation. The respective crystallographic orientations of the two notch systems are shown in Fig. 1b.

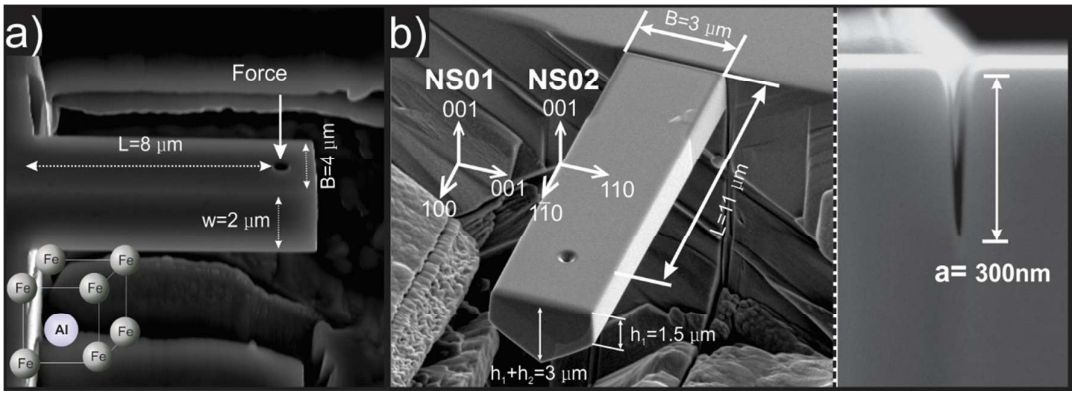

Fig. 1. The Secondary Electron (SE) micrographs of the tested cantilevers with characterized dimensions a) un-notched; b) notched.

After ex-situ EBSD characterization, two sets of bending tests were performed using the PI-85 Pico-indent system (Hysitron Inc., USA) inside the ESEM (Quanta FEG 650 ESEM, FEI Inc., USA). For un-notched cantilevers, a stationary bending was applied until a final deflection of 5 µm. For notched cantilevers, a cyclic bending with several loading/unloading segments was applied to keep track of the crack propagation, and a final deflection of 4.5 µm was selected due to the limited bottom space milled for those cantilevers. All the tests were performed under two environmental conditions, namely Vacuum (~5X10^{-4} Pa) and ESEM (water vapor: 450 Pa), which provide an in-situ H charging environment. The loading rate was 1 nm/s under displacement control mode.

2.2. *Linear elastic fracture mechanics*

The conditional fracture toughness K_{IQ} based on linear elastic fracture mechanics (LEFM) was calculated using the following equations:

$$K_{IQ} = \sigma\sqrt{\pi a} f(x) \quad (1)$$

$$\sigma = \frac{PL\bar{y}}{I} \quad (2)$$

Where σ is the nominal stress, a is the crack depth, $f(x)$ is the dimensionless geometry factor, P is the fracture load, L is the distance between the notch and the loading point, $\bar{y}$ is the distance from the upper surface to the centroid of the beam, I is the moment of inertia of the beam cross-section. For the beam geometry shown in Fig. 1b, $\bar{y}$ and I can be calculated using the following equations:

$$\bar{y} = \frac{h_1^2 + h_2(h_1 + \frac{1}{3}h_2)}{2h_1 + h_2} \quad (3)$$

$$I = \left\{\frac{Bh_1^3}{12} + Bh_1(\bar{y} - \frac{h_1}{2})^2\right\} + \left\{\frac{Bh_2^3}{36} + \frac{Bh_2}{2}(h_1 + \frac{h_2}{3} + \bar{y})^2\right\} \quad (4)$$

Where the h_1, h_2, B are the beam cross-section dimensions.

The geometry factor $f(\frac{a}{2\bar{y}})$ was calculated by Chan et. al (34) using extensive finite element simulations for a wide range of specimen geometries:

$$f(x) = 3.710x^3 - 0.630x^2 + 0.242x + 0.974 \quad (5)$$

Where the $x = \frac{a}{2\bar{y}}$ is the characteristic geometric factor.

2.3. *Evaluation of the J-integral*

If the plastic zone size is large with respect to the sample dimension, the LEFM is no longer applicable. In this case, the Elastic-Plastic Fracture Mechanics (EPFM) should be used to analyze the fracture toughness. The determination of J-integral relies on the precise knowledge of the crack propagation, which can be realized by performing several unloading segments. By measuring the unloading compliance on each unloading segment, the crack length can be calculated:

$$\bar{y} - a_i = \sqrt[3]{\frac{4k_i L^3}{BE}} \quad (6)$$

Where B is the width of the cantilever and k_i is the unloading compliance for the i-th step of unloading. The J-integral of the i-th loading/unloading part can be calculated using the following equation:

$$J_i = J_i^{el} + J_i^{pl} = \frac{K_{IQ}^2(1-v^2)}{E} + \left[J_{i-1}^{pl} + \frac{\eta(A_i^{pl} - A_{i-1}^{pl})}{B(\bar{y} - a_{i-1})}\right]\left[1 - \frac{a_i - a_{i-1}}{\bar{y} - a_{i-1}}\right] \quad (7)$$

Where K_{IQ} can be determined using Eq. (1) by setting $F_Q = F_{0.95}$ for the i-th loading part, η is a constant factor that equals to 2, v is the Poisson's ratio, and A_i^{pl} is the area beneath the load-displacement curve excludes the elastic contribution. From the complete loading/unloading curve, the J versus crack extension (the crack-resistance curve) can be deduced. The fracture toughness is calculated by:

$$K_{IQ,J} = \sqrt{J_Q \frac{E}{1-v^2}} \quad (8)$$

Where J_Q is the critical J -value educed from the crack-resistance curve. More details will be present in results and discussion part.

3. Results and Discussion

3.1. Hydrogen induced cracking on un-notched cantilevers

Fig. 2 shows the bending properties of the un-notched beams under different environmental conditions, namely Vacuum and ESEM with 450 Pa water vapor. The bending stress-strain data was estimated from the experimental load-displacement data using the Euler-Bernoulli beam theory: $\sigma = \frac{4Fy}{B \cdot w^2}$, in which F, y, w, t refer to the forces, moment arms, width and thickness of the beams, respectively. The corresponding strain, ε, was corrected by normalizing the displacement, d, with the moment arm, y. The calculated strain cannot present the real strain in the beam due to the asymmetric geometry, for that the top surface and bottom surface are not deformed identically. However, the agreement of the elastic part of the tested beams suggests that the strain can be counted as a reasonable normalization treatment.

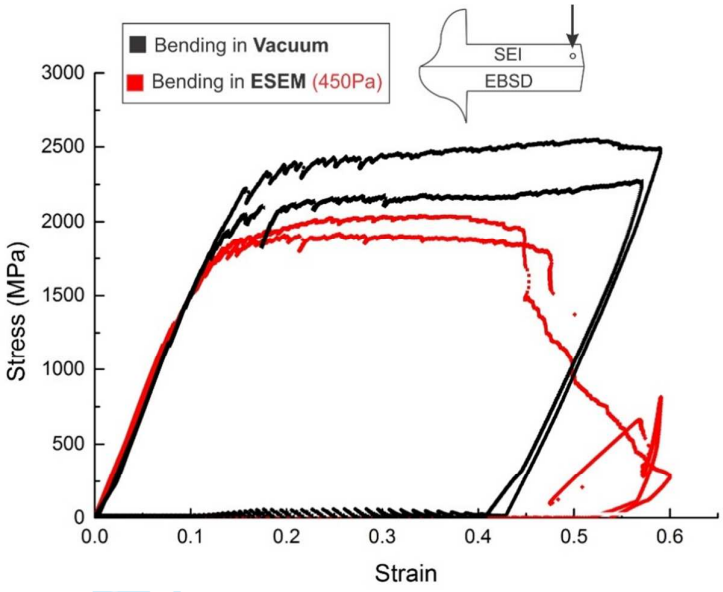

Fig. 2. Representative strain-stress curves for the beams bent in Vacuum (black ones) and ESEM 450 Pa (red ones).

The above flow curves show a clear effect of H from three following aspects: i) the elastic stiffness is not so much influenced by the presence of H. ii) The flow stress of the cantilevers bent in Vacuum condition is higher than those bent in ESEM condition. This H induced reduction in the flow stress can be easily understood within the defactant concept, which states that the defects nucleation energy will be reduced by introducing H (35-37). iii) The nucleation and propagation of a crack initiated on the transition triple corner from bulk to beam is observed as ~0.3 plastic strain, see Fig. 3b; meanwhile a reduction in bending stress is detected. For beams tested in Vacuum condition, the stress keeps a relative constant value without showing any cracking behavior until the final 5 μm beam deflection, see Fig. 3a.

The EBSD characterization method was applied on the side of the cantilevers. The Confidence Index (CI) for all the points shown here are higher than 0.1, and the points with CI lower than 0.1 are simply colored in black. The low CI values at the bottom part of the cantilever in Fig. $3b_3$ are due to the cracking induced out-of-plane bending, which introduces deflection from the normal 70^o tilting for EBSD that affects the signal collection. Therefore, here we only compare the reliable EBSD data from the upper parts of the beams to interpret our results. The local misorientation gradients are shown by the corresponding Kernel Average Misorientation (KAM) maps, which qualify the average misorientation of each EBSD point with respect to its 3^{rd} nearest neighbors, and by which it gives information about the distribution of geometrically necessary dislocations (GNDs). The KAM information for cantilevers bent in Vacuum and ESEM are shown in Fig. $3a_3$ and Fig.$3b_3$, respectively.

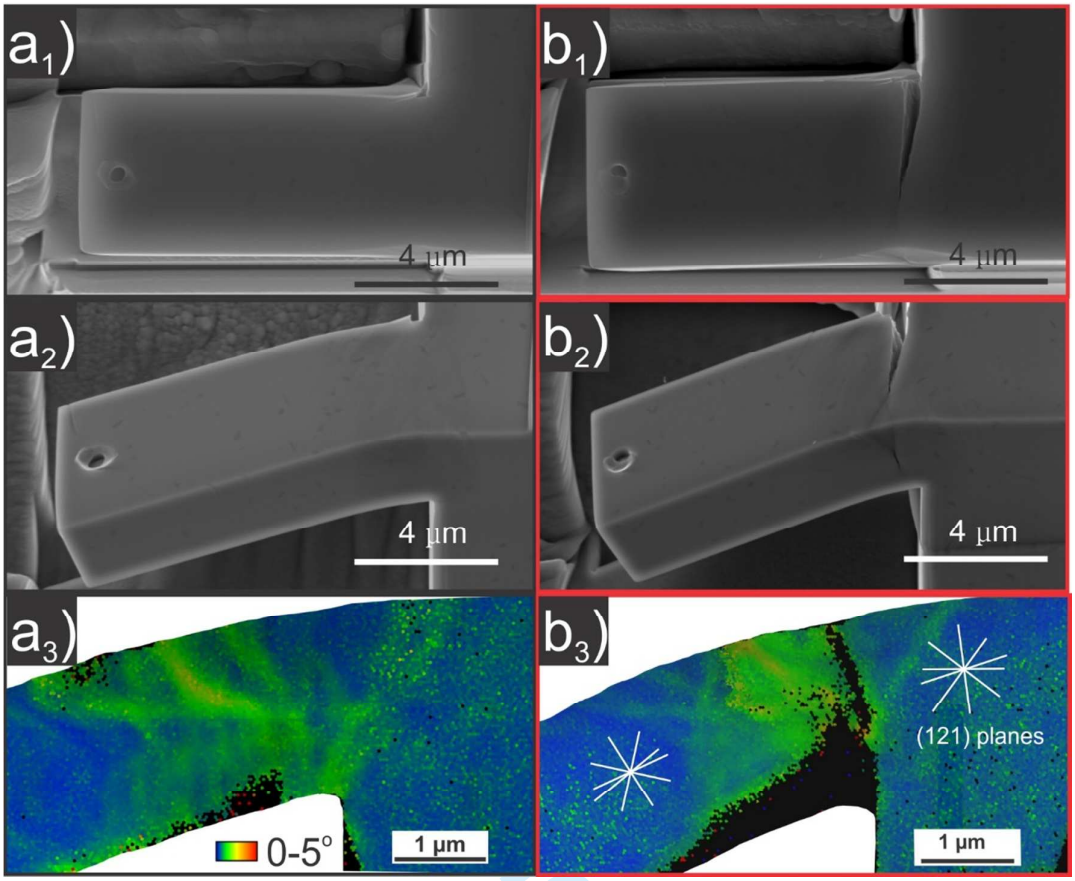

Fig. 3. SE micrographs of the top view and side view of the beams bent in Vacuum a_1) a_2) and ESEM 450 Pa b_1) b_2), showing the crack initiates on the corner of the beam and propagates towards the outer surface. EBSD characterization with the corresponding KAM analysis from the outer surface for both conditions a_3) and b_3) show a strong stain localization for beam bent in ESEM.

The following features can be summarized by comparing the KAM maps for the two cases: i) the orientation changes are not homogeneous but forming a localized zone near to the transition corner from the bulk to the beam, which indicates the beams are not deformed in the ideal bending manner. ii) The plastic zone is more localized to the cracking region for ESEM case, while for Vacuum case, a wider and homogeneous dislocation distribution is observed. The H induced localized plastic zone near to the cracking area has been observed previously in austenitic stainless steels (38, 39), in which the slip traces were concentrated around the fatigue crack area when the sample was deformed under H charged condition. iii) A wavier pattern is observed in the beam bent in Vacuum, while in ESEM case, the slip traces are found more planar along certain slip planes. The planar slip manner is frequently observed in FeAl B2 alloys with lower Al compositions (<36 at. %), in which the Anti-Phase Boundary (APB) energy is low, and the dislocation configuration consists of two $\frac{1}{2}a_0$<111> partial dislocations connected by a $\frac{1}{2}a_0$<111> APB. As increasing in Al concentration to reach the stoichiometric composition, the B2 APB energy increases so that the pair of partial dislocations cannot stay separated and merge into one single dislocation a_0<111>, which makes the cross-slip easier and promotes a wavier slip traces. The appearance of planar slip traces for ESEM case may associate with a reduced APB energy under H exposure, which resembles the similar effect occurring in some FCC alloy systems that H will reduce the stacking fault energy thus promoting planar slip (40-42).

3.2. Orientation effect on the hydrogen induced cracking

To better understand the H induced cracking behavior, the cantilever design used in the section above is modified by adding a notch on the top surface to introduce stress concentration. Moreover, two notch systems with notch plane on (010) and (110) crystallographic planes, as shown in Fig. 1b, were tested in this work.

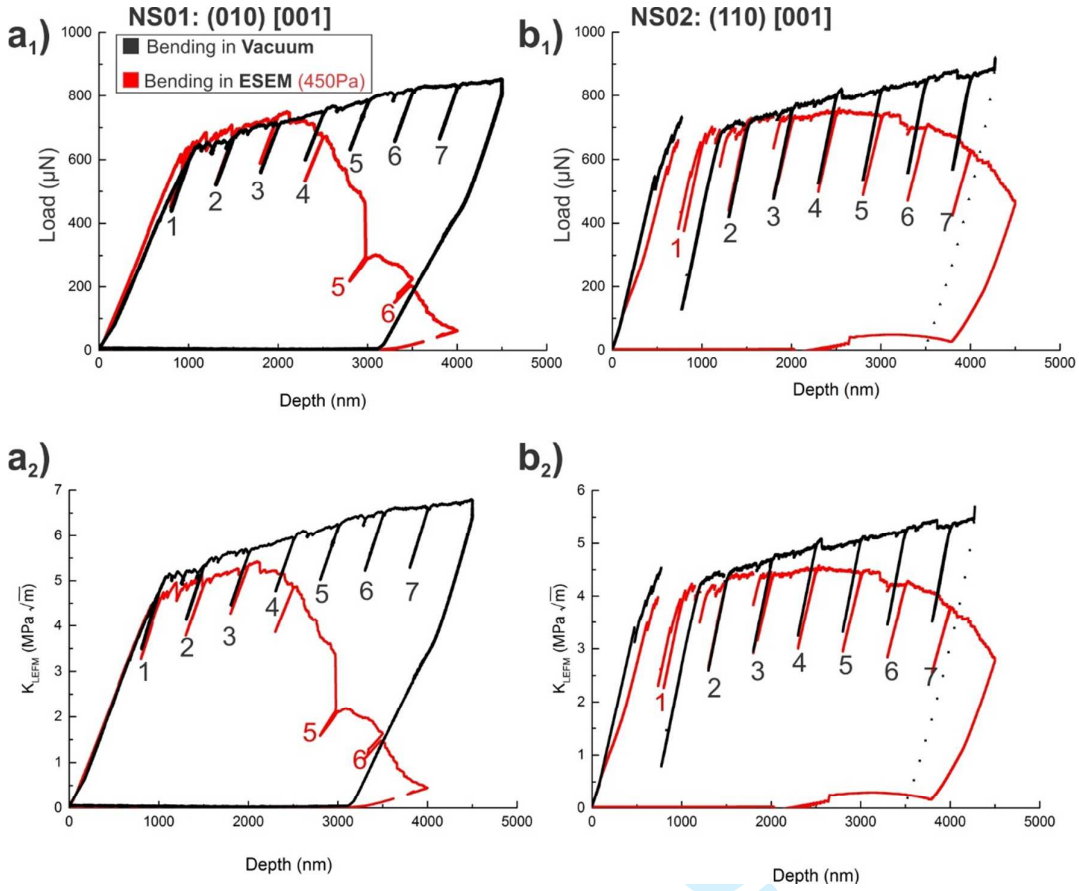

Fig. 4. Experimental load-displacement curves for the beams with (010) [001] a_1) and (110) [001] b_1) notch systems bent in Vacuum (black ones) and ESEM 450 Pa (red ones), and the corresponding stress intensity factors at the crack tip based on LEFM a_2) and b_2).

Fig. 4 shows the experimental load-displacement curves for beams with two notch systems bent in Vacuum and ESEM states. For both notch orientations, we observed a continuous increase in bending load and a relative constant stiffness in each unloading segment when beams bent under Vacuum condition, while for beams bent under ESEM condition, the bending force would reach a more or less force plateau, and followed by a decrease around certain amount of deflection. The force plateau is reached by two opposite effects. The plasticity ahead of the crack tip introduces hardening effect meanwhile the reduction of the cross-section area associated with the crack propagation reduces the total bending force. After the first drop in the unloading stiffness, which happened at the 2nd unloading segment for both notch systems, the stiffness continuously decreases during the whole experiment. The decrease in unloading stiffness is linked to the crack length extension, which has been proven by in-situ SEM observation and by testing on un-notched cantilevers(43). Despite the similar points mentioned above, some differences have been observed between the two

notch orientations. The stiffness found in NS01 is considerably higher than that of NS02, which is due to the difference in the elastic moduli with two different orientations ($E_{(010)} = 210\ GPa, E_{(110)} = 316\ GPa$) (44). After the force plateau, the bending force is falling sharply associated with a rapid crack growth for NS01, while a continued steady decline in force for NS02, indicating a slower crack extension compared to NS01. Due to the difference in cross-section on the top and bottom of the cantilever, once the crack passes the upper rectangular part into the triangular part, an abrupt shrinkage in the cantilever cross-section will cause a sudden drop in the bending force. This occurred in NS01 sample in the middle of the 4th and 5th unloading segments where a sudden load drop is detected.

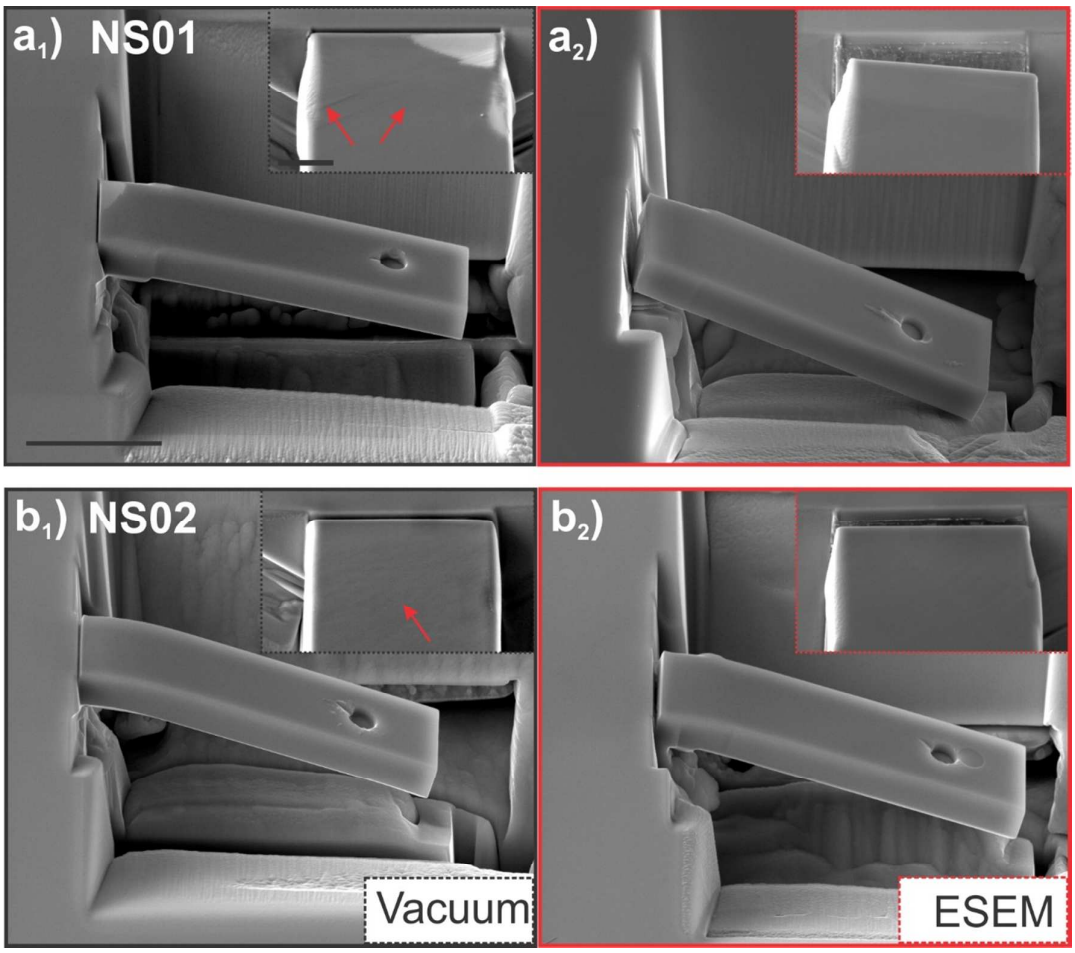

Fig. 5. SE micrographs of the cantilevers with two notch systems NS01 a) and NS02 b) bent in Vacuum (black frame) and ESEM (red frame) conditions. The arrows point the slip traces on the top surface. The scale bars on the side view and on the top view micrographs are 5 µm and 1 µm, respectively.

Fig. 5 shows the micrographs of the beams after testing. For Vacuum case, no crack extension is observed from the side view, and the deflection is mainly consumed by the plastic deformation at the root of the cantilever. Notch blunting and obvious slip traces on the top surface are observed. For ESEM condition, an apparent crack opening is observed from side view while no recognizable slip traces are shown on the top surface of the beam, indicating that cracking consumes most of the beam deflection. A large extension of the crack in NS01 sample where the crack has passed almost the whole beam thickness is

observed, while after the same deflection, the crack in NS02 sample reaches roughly half of the beam thickness, shown in Fig. $5a_2$ and $5b_2$.

The stress intensity factor is estimated by applying the LEFM approach. By using the equations addressed in the previous experimental procedure part, the load is normalized into the stress intensity factor (K_{LEFM}) with respect to the sample geometry. Graphs of K_{LEFM} as a function of the bending depth for two notch systems are shown in Fig. $4a_2$ and $4b_2$. By considering the 3rd unloading/loading as the initiation of the cracking, the K_{LEFM} for two notch systems can be estimated: $K_{LEFM,(010)}$= 5.32 MPa√m and $K_{LEFM,(110)}$= 4.42 MPa√m. In order the calculated LEFM fracture toughness to be applicable to qualify the material's properties, the plastic zone should be relatively smaller than the tested sample geometry. The plastic zone size can be estimated by the Irwin approximation: $t_1 = \frac{K_{IC}^2}{3\pi\sigma_Y^2}$, where K_{IC} is the critical stress intensity of the material for fracture in mode I and σ_Y is the yield strength. The ASTM standards give a lower limit of the sample thickness by: $t_2 = 2.5\frac{K_{IC}^2}{\sigma_Y^2}$(45). For samples thinner than t_1, the plane-stress value of fracture toughness is measured, while plane strain fracture toughness requires that both specimen thickness B, and crack length a above a critical thickness, t_2. Considering a macroscopic yield stress of 400 MPa for FeAl (100) single crystal(29), the respective size calculated for NS01 is: $t_1 = 18\,\mu m$ and $t_2 = 440\,\mu m$, which gives the sample size two orders of the tested geometry. The overestimation of the sample size may relate to the underestimation of the yield strength, which will increase with decreasing testing geometry owing to the size effect. Since the tested beams do not fulfill the geometry requirements from ASTM standards, the K_{LEFM} present here can only be used for comparison while the exact values obtained cannot count as valid fracture properties. Moreover, since neither crack propagation nor large-scale yielding is taken into consideration in LEFM, the depiction of K_{LEFM} in Fig.4 only shows the lower limits of the real values.

A smaller fracture toughness of (010) notch plane than that of (110) notch plane is obtained, which is opposite to the observations from the previous research both from macroscopic four-point bending tests and theoretical calculations (46, 47). This inconsistency comes from the overlook of the contribution from the plasticity before the crack propagation actually happened. This drawback can be suppressed by applying the EPFM models (J-integral or Crack Mouth Opening Displacement), which takes the plasticity before cracking into the calculation of the fracture toughness.

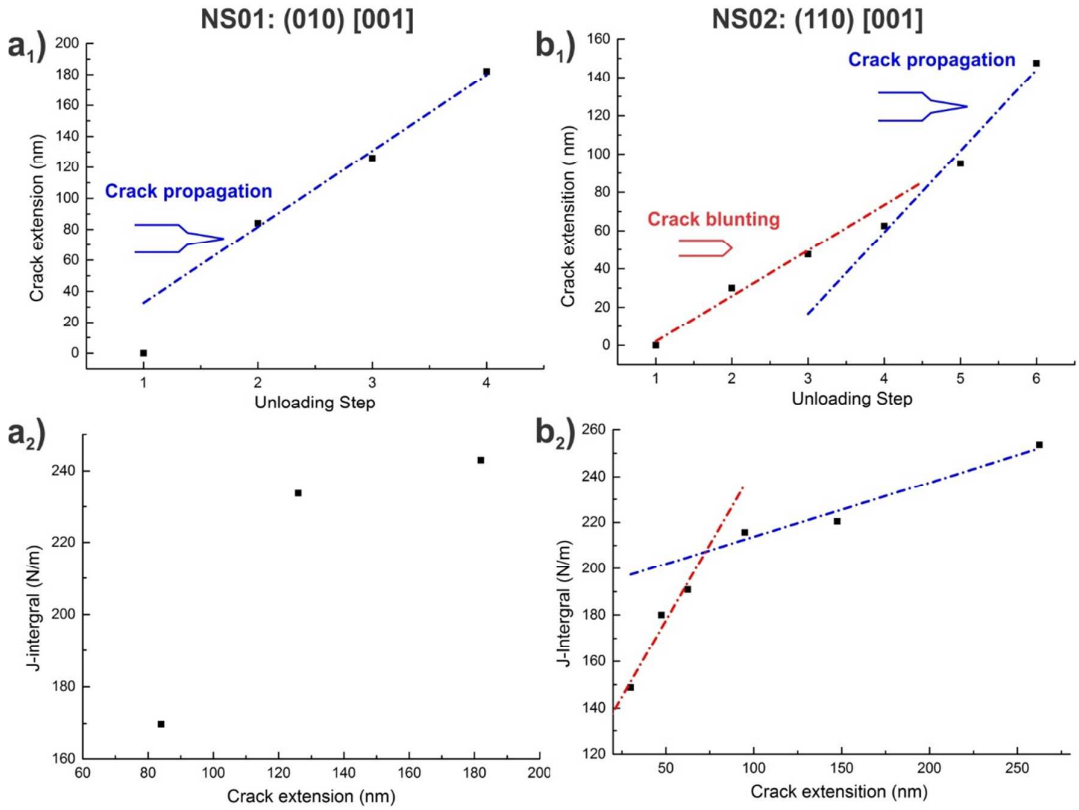

Fig. 6. The crack extension calculated by the unloading compliances for beams with (010) [001] a_1) and (110) [001] b_1) notch systems bent in ESEM 450 Pa, the J-integral versus the crack extension for the same beams a_2) and b_2).

To determine the fracture toughness from the J-integral method, a pronounced knowledge of crack extension during experiment is required. The crack length at each unloading point is obtained by using Eq. (6), and the corresponding results are shown in Fig. $6a_2$ and $6b_2$. For NS02, it is obvious that two different stages of crack propagation with different propagating rates are present during the experiment. The crack blunting is more responsible for the 1st stage and the sharp crack propagation happened at the 2nd stage. While for NS01, a large crack extension is measured at the 2nd unloading segment, suggesting that the crack blunting effect is much less than that for NS02. Taken (010) as the cleavage plane for FeAl with stoichiometric composition, this observation keeps consistency with the previous research showing that crack blunting is more pronounced while a misalignment occurred between the crack plane and the cleavage plane (46).The J-integral is calculated for each loading/unloading segment using Eq. (7). The J versus crack extension curves for each condition are shown in Fig. $6a_2$ and $6b_2$. For the NS01 sample, a large crack extension happened before the 2nd unloading segment, and a proper way to evaluate the J_Q is to choose this point as the starting of the crack propagation. The J_Q obtained here can be considered as the uppermost value, since obviously the crack propagation started before the 2nd unloading. For the beam with NS02 orientation, the critical J_Q values can be obtained by fitting the data with two linear functions, in which the 1st linear function depicts the crack blunting effect and the 2nd one describes the crack growth. By selecting the start points of the crack propagation, the fracture toughness can be calculated according to Eq. (8): $K_{J\text{-}Integral,(010)}$= 6.92 MPa√m and $K_{J\text{-}Integral,(110)}$= 8.68 MPa√m. For cantilevers bent in Vacuum

condition, the fracture toughness are calculated by taking all the plastic area under the load-depth curve: $K_{J\text{-}Integral,(010)} > 15.8$ MPa√m and $K_{J\text{-}Integral,(110)} > 18.9$ MPa√m. Since no crack propagation was observed in Vacuum case for both notch systems, the real fracture toughness should be higher than the calculated values. In order to qualify the applicability of the above obtained conditional fracture toughness, certain geometry restricts should be fulfilled(48):

$$ligament, W > \frac{25 J_{IC}}{\sigma_Y}$$

Considering a macroscopic yield strength of 400 MPa for FeAl (100) single crystal, together with the J-value for the 2nd unloading segment of 169 N/m, the smallest applicable dimension is calculated to be 10 µm. This requirement is not met by a factor of 3. However, one should always take into consideration of the size effect that a decrease in sample size will introduce an increase in the strength, which will relax this requirement to small test geometries. Since no reliable yield strength data at small scale are available, the applicability of the fracture toughness obtained here is still under question. Nevertheless, the conditional fracture toughness can still be used for comparing the results.

4. Summary

The H assisted cracking phenomenon in FeAl intermetallic alloys was analyzed with the in-situ micro cantilever-bending test within environmental scanning electron microscope. Two sets of cantilevers were tested in this work: cantilevers without notch, cantilevers with notch laying on (010) plane and (110) plane. The main findings are:

1. The FeAl single crystalline material with B2 ordered structure is intrinsically ductile, even with stoichiometric composition. The loss of ductility at room temperature is mainly due to the presence of H.
2. For notched cantilevers, H is found to reduce the bending strength and the ductility, to enhance the crack nucleation and propagation, and to localize the plastic zone near the crack area.
3. For un-notched cantilevers, H is found to reduce the fracture toughness and to initiate cracking for both studied notch systems.
4. The conditional critical stress intensity factor obtained by J-integral for the cantilever with (010) notch plane is $K_{J\text{-}Integral,(010)}$= 6.92 MPa√m; with (110) notch plane is $K_{J\text{-}Integral,(110)}$= 8.68 MPa√m. Samples with notch plane parallel to the (010) cleavage plane are found to be more fragile to HE.

Acknowledgements

This research was supported by the Research Council of Norway through the projects of HIPP under the project number 234130/E30 and HyF-Lex (244068/E30). The Research Council of Norway is acknowledged for support to NTNU NanoLab through the Norwegian Micro- and Nano-Fabrication Facility, Norfab (197411/V30).

1. W.H.Johnson, editor. Proceedings of the Royal Society of London; 1855.
2. Shih DS, Robertson IM, Birnbaum HK. Hydrogen embrittlement of α titanium: In situ tem studies. Acta Metallurgica. 1988;36(1):111-24.

3. Varvenne C, Mackain O, Proville L, Clouet E. Hydrogen and vacancy clustering in zirconium. Acta Materialia. 2016;102:56-69.
4. Coleman CE, Hardie D. The hydrogen embrittlement of α-zirconium—A review. Journal of the Less Common Metals. 1966;11(3):168-85.
5. Weekes HE, Vorontsov VA, Dolbnya IP, Plummer JD, Giuliani F, Britton TB, et al. In situ micropillar deformation of hydrides in Zircaloy-4. Acta Materialia. 2015;92:81-96.
6. Weekes HE, Jones NG, Lindley TC, Dye D. Hydride reorientation in Zircaloy-4 examined by in situ synchrotron X-ray diffraction. Journal of Nuclear Materials. 2016;478:32-41.
7. Troiano AR, Gibala R, Hehemann R. Hydrogen embrittlement and stress corrosion cracking: a Troiano Festschrift: ASM International; 1984.
8. Vehoff H, Neumann P. Crack propagation and cleavage initiation in Fe-2.6%-Si single crystals under controlled plastic crack tip opening rate in various gaseous environments. Acta Metallurgica. 1980;28(3):265-72.
9. Vehoff H, Rothe W. Gaseous hydrogen embrittlement in FeSi- and Ni-single crystals. Acta Matallurgica. 1983;31:13.
10. Tarzimoghadam Z, Ponge D, Klöwer J, Raabe D. Hydrogen-assisted failure in Ni-based superalloy 718 studied under in situ hydrogen charging: The role of localized deformation in crack propagation. Acta Materialia. 2017;128:365-74.
11. Wang M, Tasan CC, Koyama M, Ponge D, Raabe D. Enhancing Hydrogen Embrittlement Resistance of Lath Martensite by Introducing Nano-Films of Interlath Austenite. Metall and Mat Trans A. 2015;46(9):3797-802.
12. Lynch S. Hydrogen embrittlement phenomena and mechanisms. Corrosion Reviews. 2012;30(3-4).
13. Lynch SP. Environmentally assisted cracking: Overview of evidence for an adsorption-induced localised-slip process. Acta Metallurgica. 1988;36(10):2639-61.
14. Robertson IM, Sofronis P, Nagao A, Martin ML, Wang S, Gross DW, et al. Hydrogen Embrittlement Understood. Metallurgical and Materials Transactions B. 2015;46(3):1085-103.
15. Song J, Curtin WA. Atomic mechanism and prediction of hydrogen embrittlement in iron. Nature materials. 2013;12(2):145-51.
16. Song J, Curtin WA. Mechanisms of hydrogen-enhanced localized plasticity: An atomistic study using α-Fe as a model system. Acta Materialia. 2014;68:61-9.
17. Xie D, Li S, Li M, Wang Z, Gumbsch P, Sun J, et al. Hydrogenated vacancies lock dislocations in aluminium. Nature communications. 2016;7:13341.
18. Hatano M, Fujinami M, Arai K, Fujii H, Nagumo M. Hydrogen embrittlement of austenitic stainless steels revealed by deformation microstructures and strain-induced creation of vacancies. Acta Materialia. 2014;67:342-53.
19. Ziegler N. Resistance of iron-aluminum alloys to oxidation at high temperatures. Trans Am Inst Min Met Eng. 1932;100:267-71.
20. McKamey CG, Horton JA. The effect of molybdenum addition on properties of iron aluminides. MTA. 1989;20(4):751-7.
21. Li X, Scherf A, Heilmaier M, Stein F. The Al-Rich Part of the Fe-Al Phase Diagram. Journal of Phase Equilibria and Diffusion. 2016;37(2):162-73.
22. Stoloff NS, Davies RG. The plastic deformation of ordered FeCo and Fe3 Al alloys. Acta Metallurgica. 1964;12(5):473-85.
23. Baker I, Li X, Xiao H, Carleton R, George EP. The room temperature strengthening effect of boron as a function of aluminum concentration in FeAl. Intermetallics. 1998;6(3):177-83.
24. Radhakrishna A, Baligidad RG, Sarma DS. Effect of carbon on structure and properties of FeAl based intermetallic alloy. Scripta Materialia. 2001;45(9):1077-82.
25. Baligidad RG, Prakash U, Radhakrishna A, Rao VR, Rao PK, Ballal NB. Effect of carbides on embrittlement of Fe3Al based intermetallic alloys. Scripta Materialia. 1997;36(6):667-71.
26. Klein O, Baker I. Effect of heat-treatment on the tensile behavior of iron-rich FeAl and FeAl + B. Scripta Metallurgica et Materialia. 1994;30(5):627-32.

27. Liu CT, George EP. Environmental embrittlement in boron-free and boron-doped FeAl (40 at. % Al) alloys. Scripta Metallurgica et Materialia. 1990;24(7):1285-90.
28. Di Stefano D, Nazarov R, Hickel T, Neugebauer J, Mrovec M, Elsässer C. First-principles investigation of hydrogen interaction with TiC precipitates in $\ensuremath{\alpha}$-Fe. Physical Review B. 2016;93(18):184108.
29. Specht P, Brede M, Neumann P. Fracture Toughness, Fracture Planes and BDT in Stoichiometric Feal and Nial Single Crystals. MRS Proceedings. 1994;364.
30. Fu C, Painter G. First principles investigation of hydrogen embrittlement in FeAl. Journal of Materials Research. 1991;6(04):719-23.
31. Li JCM, Liu CT. Crack nucleation in hydrogen embrittlement. Scripta Metallurgica et Materialia. 1992;27(12):1701-5.
32. Deng Y, Hajilou T, Wan D, Kheradmand N, Barnoush A. In-situ micro-cantilever bending test in environmental scanning electron microscope: Real time observation of hydrogen enhanced cracking. Scripta Materialia. 2017;127:19-23.
33. Hajilou T, Deng Y, Rogne BR, Kheradmand N, Barnoush A. In situ electrochemical microcantilever bending test: A new insight into hydrogen enhanced cracking. Scripta Materialia. 2017;132:17-21.
34. Chan H, Roberts SG, Gong J. Micro-scale fracture experiments on zirconium hydrides and phase boundaries. Journal of Nuclear Materials. 2016;475:105-12.
35. Kirchheim R. On the solute-defect interaction in the framework of a defactant concept. International Journal of Materials Research. 2009;100(4):483-7.
36. Kirchheim R. Revisiting hydrogen embrittlement models and hydrogen-induced homogeneous nucleation of dislocations. Scripta Materialia. 2010;62(2):67-70.
37. Kirchheim R, Somerday B, Sofronis P. Chemomechanical effects on the separation of interfaces occurring during fracture with emphasis on the hydrogen-iron and hydrogen-nickel system. Acta Materialia. 2015;99:87-98.
38. Murakami Y, Kanezaki T, Mine Y, Matsuoka S. Hydrogen Embrittlement Mechanism in Fatigue of Austenitic Stainless Steels. Metall and Mat Trans A. 2008;39(6):1327.
39. Kanezaki T, Narazaki C, Mine Y, Matsuoka S, Murakami Y. Effects of hydrogen on fatigue crack growth behavior of austenitic stainless steels. International Journal of Hydrogen Energy. 2008;33(10):2604-19.
40. Pontini AE, Hermida JD. X-Ray diffraction measurement of the stacking fault energy reduction induced by hydrogen in an AISI 304 steel. Scripta Materialia. 1997;37(11):1831-7.
41. Robertson IM. The effect of hydrogen on dislocation dynamics. Engineering Fracture Mechanics. 2001;68(6):671-92.
42. Rozenak P, Robertson IM, Birnbaum HK. HVEM studies of the effects of hydrogen on the deformation and fracture of AISI type 316 austenitic stainless steel. Acta Metallurgica et Materialia. 1990;38(11):2031-40.
43. Ast J, Merle B, Durst K, Göken M. Fracture toughness evaluation of NiAl single crystals by microcantilevers—a new continuous J-integral method. Journal of Materials Research. 2016:1-9.
44. Fu CL, Yoo MH. Deformation behavior of B2 type aluminides: FeAl and NiAl. Acta Metallurgica et Materialia. 1992;40(4):703-11.
45. E 399-490: Standard Test Method for Plane-Strain Fracture

Toughness of Metallic Materials. ASTM International, West Conshohocken, PA1997.
46. Chang K-M, Darolia R, Lipsitt H. Cleavage fracture in B2 aluminides. Acta metallurgica et materialia. 1992;40(10):2727-37.
47. Li T, Morris JW, Chrzan DC. Ab initio. Physical Review B. 2006;73(2):024105.
48. E1820: Standard Test Method for Measurement of Fracture Toughness

ASTM International, West Conshohocken, PA

1997.

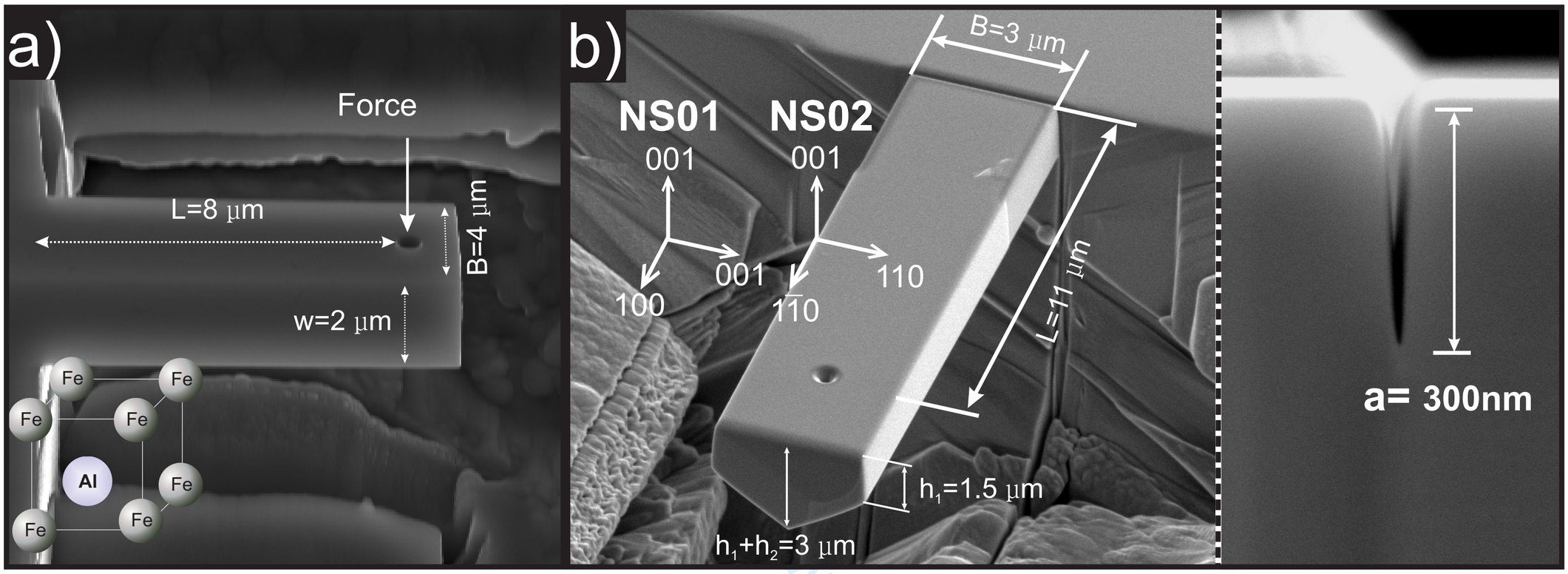

Fig. 1. The Secondary Electron (SE) micrographs of the tested cantilevers with characterized dimensions a) un-notched; b) notched.

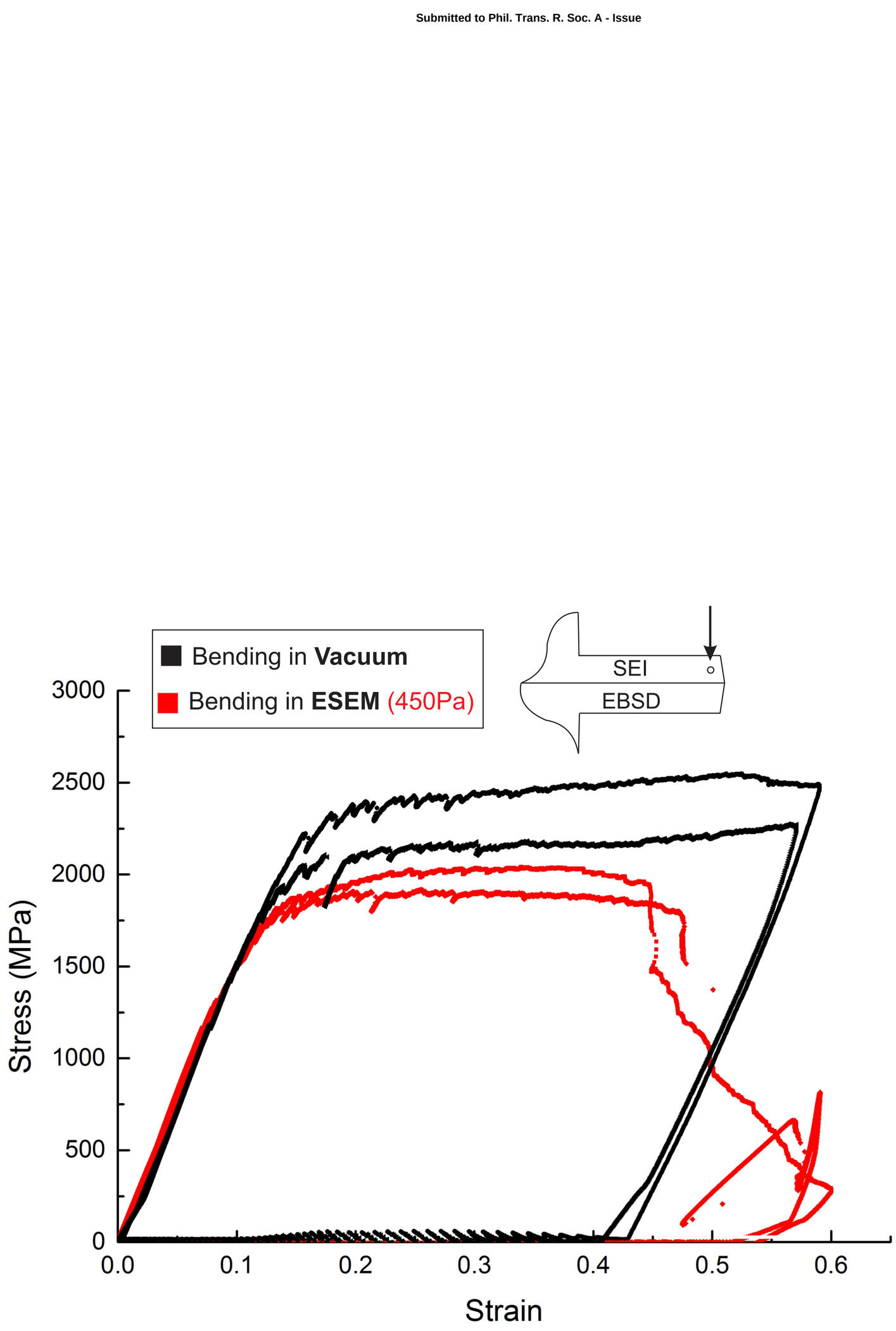

Fig. 2. Representative strain-stress curves for the beams bent in Vacuum (black ones) and ESEM 450Pa (red ones).

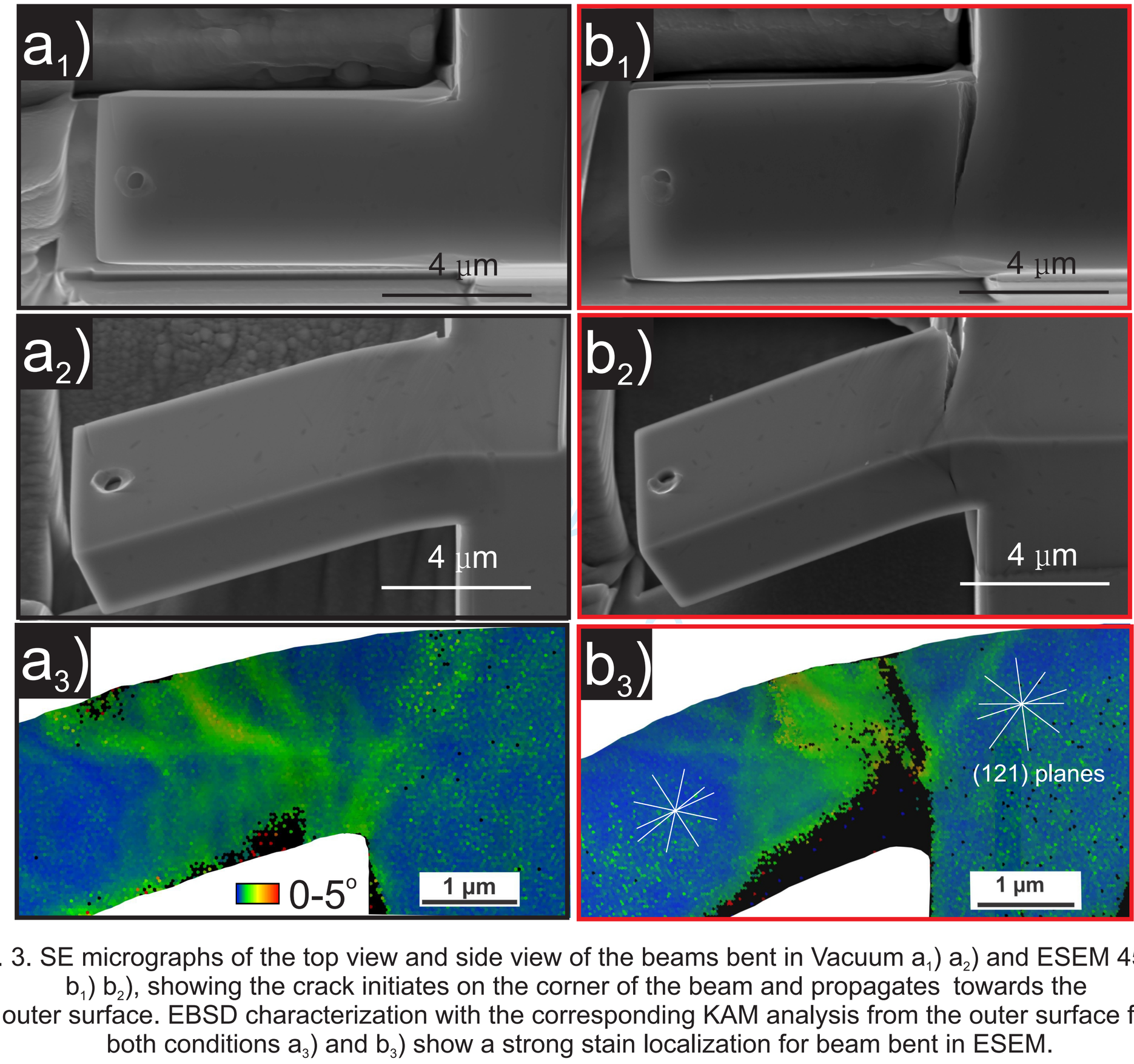

Fig. 3. SE micrographs of the top view and side view of the beams bent in Vacuum a_1) a_2) and ESEM 450Pa b_1) b_2), showing the crack initiates on the corner of the beam and propagates towards the outer surface. EBSD characterization with the corresponding KAM analysis from the outer surface for both conditions a_3) and b_3) show a strong stain localization for beam bent in ESEM.

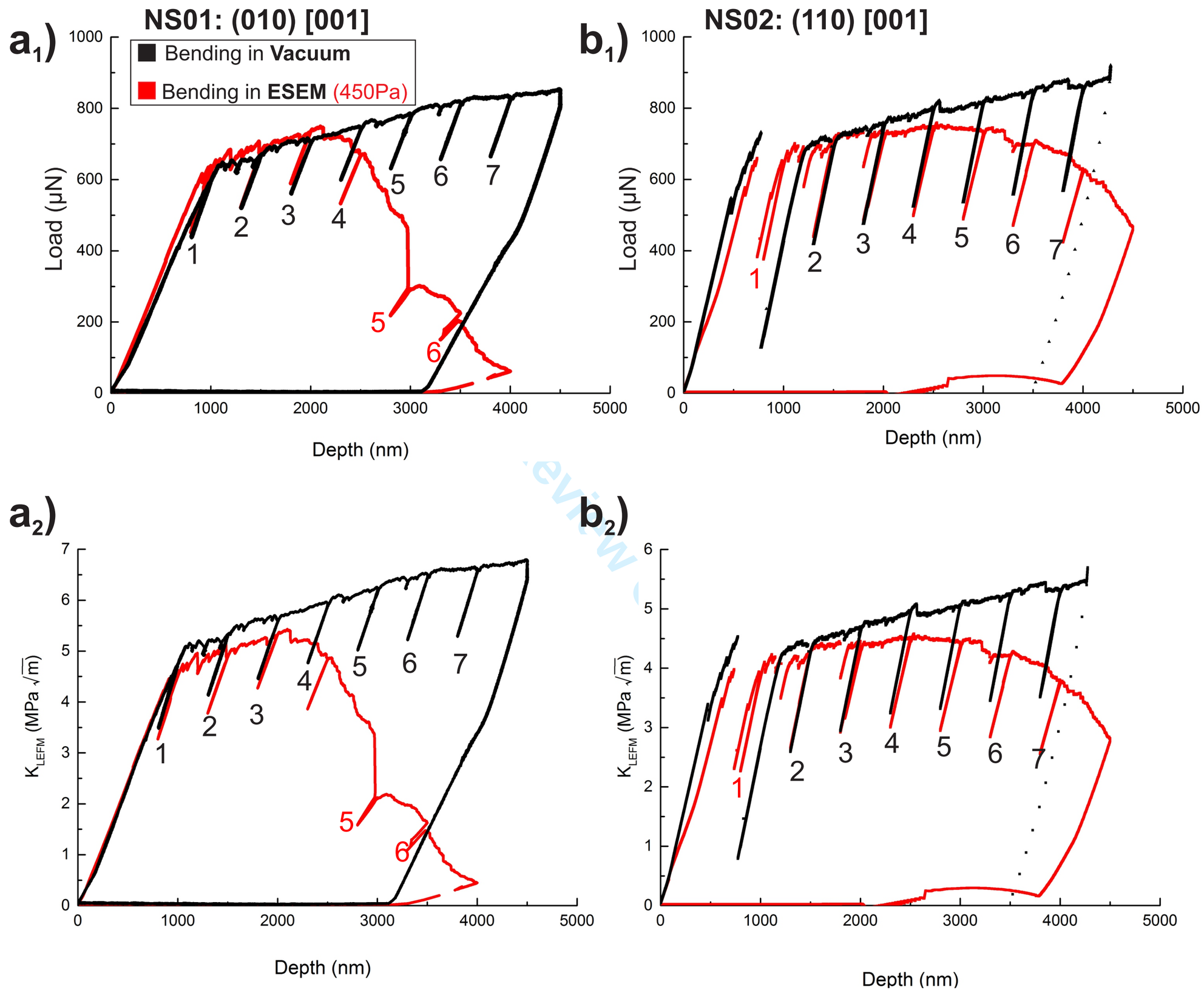

Fig. 4. Experimental load-displacement curves for the beams with (010) [001] a_1) and (110) [001] b_1) notch systems bent in Vacuum (black ones) and ESEM 450 Pa (red ones), and the corresponding stress intensity factors at the crack tip based on LEFM a_2) and b_2).

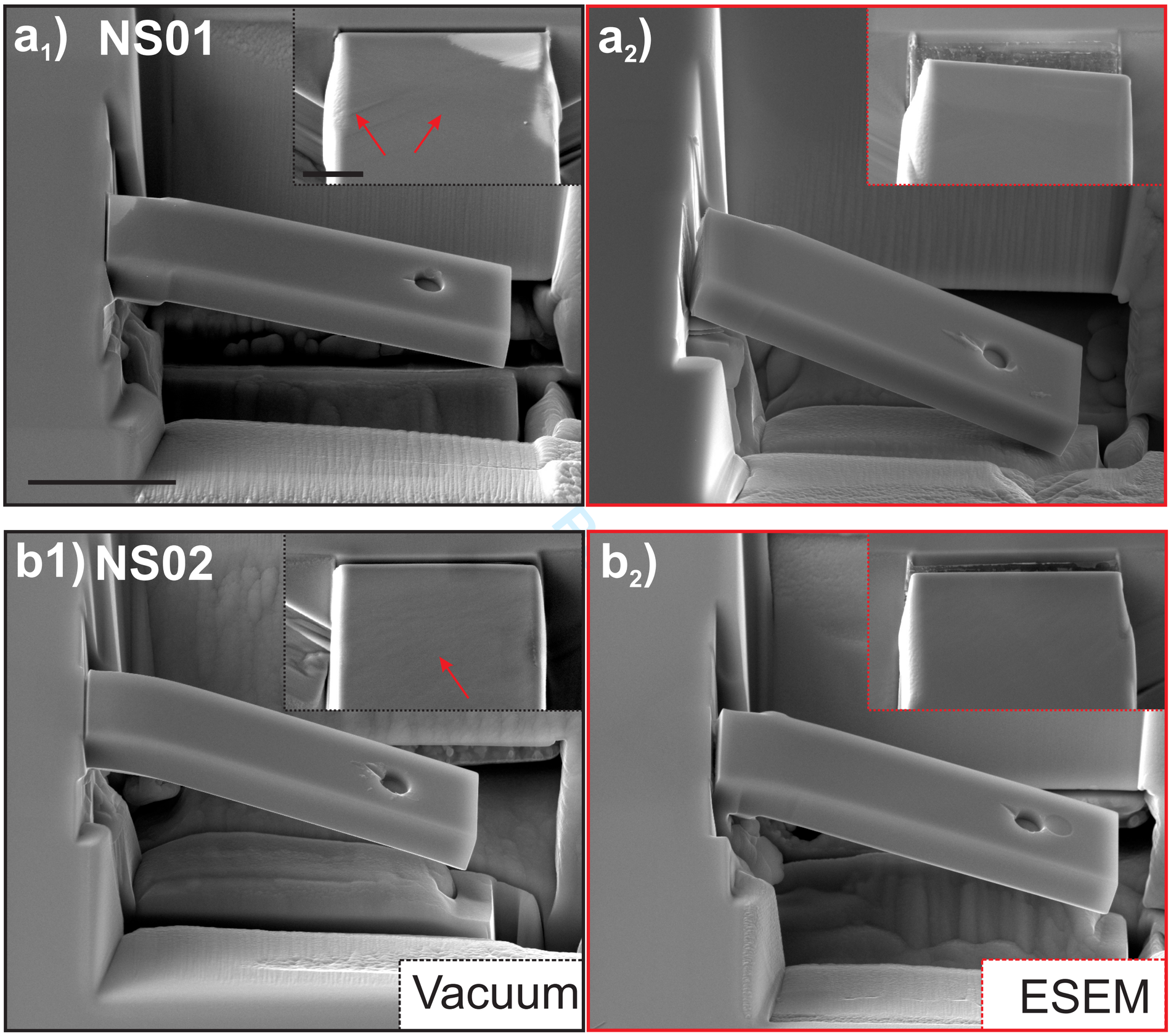

Fig. 5. SE micrographs of the cantilevers with two notch systems NS01 a) and NS02 b) bent in Vacuum (black frame) and ESEM (red frame) conditions. The arrows point the slip traces on the top surface. The scale bars on the side view and on the top view micrographs are 5 μm and 1 μm, respectively.

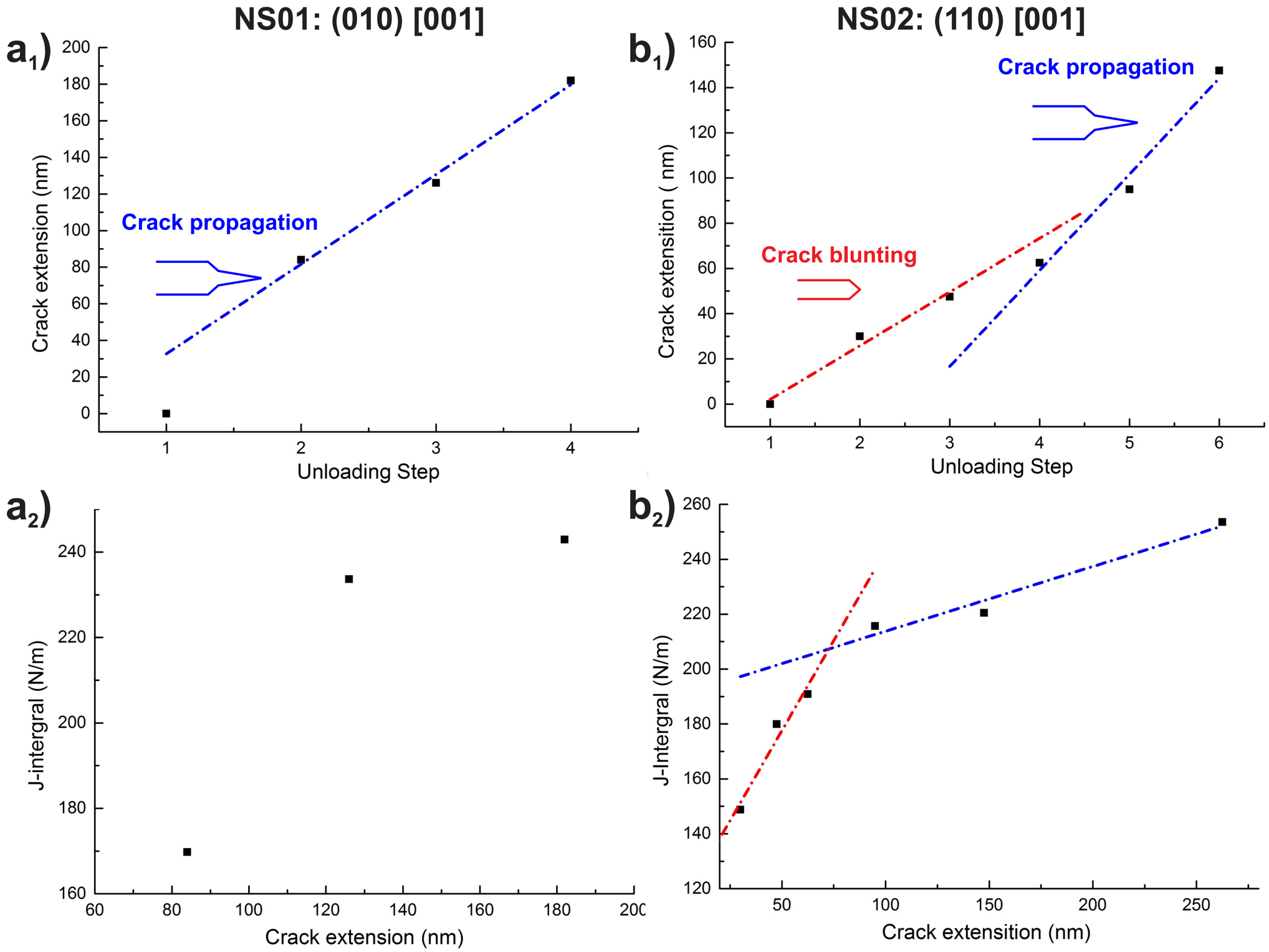

Fig. 6. The crack extension calculated by the unloading compliance for beams with (010) [001] a_1) and (110) [001] b_1) notch systems bent in ESEM 450 Pa, the J-integral versus the crack extension for the same beams a_2) and $b_{2)}$.